Available online at www.sciencedirect.com
SCIENCE DIRECT
Journal of Magnetic Resonance 179 (2006) 64–72
JMR Journal of Magnetic Resonance
www.elsevier.com/locate/jmr

A comparison of three SPRITE techniques for the quantitative 3D imaging of the ^{23}Na spin density on a 4T whole-body machine

S. Romanzetti [a], M. Halse [b], J. Kaffanke [a], K. Zilles [a,c], B.J. Balcom [b], N.J. Shah [a,c,d,*]

[a] Institute of Medicine, Research Centre Jülich, 52425 Jülich, Germany
[b] Department of Physics, University of New Brunswick, Fredericton, E3B 5A3 New Brunswick, Canada
[c] Brain Imaging Centre West, 52425 Jülich, Germany
[d] Institute of Physics, University of Dortmund, 44221 Dortmund, Germany

Received 1 February 2005; revised 11 November 2005
Available online 1 December 2005

Abstract

Sodium density maps acquired with three SPRITE-based methods have been compared in terms of the resulting quantitative information as well as image quality and acquisition times. Consideration of factors relevant for the clinical implementation of SPRITE shows that the Conical-SPRITE variant is preferred because of a 20-fold reduction in acquisition time, slightly improved image quality, and no loss of quantitative information. The acquisition of a 3D data set ($32 \times 32 \times 16$; FOV $= 256 \times 256 \times 160$ mm) for the quantitative determination of sodium density is demonstrated. In vivo Conical-SPRITE ^{23}Na images of the brain of a healthy volunteer were acquired in 30 min with a resolution of $7.5 \times 7.5 \times 7.5$ mm and a signal-to-noise ratio of 23 in cerebrospinal fluid and 17 in brain tissue.

Keywords: Sodium; Quadrupolar interaction; SPRITE

1. Introduction

The sodium ion has a fundamental role in the physiology of living tissues and is involved in a vast number of functions taking place at the cellular level. Translocation of amino acids and metabolites inside the cell or signal transduction in nerves are just a few examples among many where the presence of sodium is critical. Perhaps the most important mechanism involving the sodium ion is sodium ion homeostasis. This mechanism, in which the sodium concentration inside the cell is maintained at 10–20 mM while in the extracellular compartment is kept at about 150 mM, serves as the basis of the maintenance of the concentration gradient across the cell membrane and is responsible for the normal resting potentials and functions of cells. The basis of sodium homeostasis is the integral membrane protein Na^+, K^+-ATPase (the sodium–potassium pump), which during its normal function utilizes ATP as a driving force to pump three sodium ions out of the cell and two potassium ions inside the cell [1]. Previous estimates showed that the utilisation of as much as 23% of ATP in humans at rest is due to the sodium–potassium pump [2].

Changes in sodium concentration are indicative of diseases that alter the cell function or that are responsible for metabolic changes. Therefore, ischemia, stroke, and cancer are examples of diseases that can be readily interpreted by the local concentration change of sodium [3].

For this reason, and due to its presence in relatively high concentrations in living tissues, sodium is a very attractive nucleus to observe using MRI [4–12]. However, being a nucleus with a spin of $I = 3/2$, it has a large quadrupolar moment and therefore has a fast-relaxing component in restricted environments [13,14]. Conventional imaging

* Corresponding author. Fax: +49 2461 61 2820.
E-mail address: n.j.shah@fz-juelich.de (N.J. Shah).

1090-7807/$ - see front matter © 2005 Elsevier Inc. All rights reserved.
doi:10.1016/j.jmr.2005.11.007

sequences are ill-suited for the observation of the sodium fast-decaying component and, therefore, unconventional imaging strategies are required [6,7,10,11].

In this paper, we present an approach for sodium imaging based on MRI of solids, i.e., SPRITE imaging. This imaging sequence, developed over the past few years for the observation of non-biological samples [15–20], has proved to have an intrinsically high sensitivity to fast-relaxing species. However, since SPRITE suffers from long acquisition times, alternative centric k-space trajectories have been developed in order to speed up the acquisition and to optimize the use of the available longitudinal magnetization [21,22]. SPRITE-based methods offer a number of advantages which include immunity from susceptibility artefacts and magnetic field inhomogeneity, acquisition of the signal following a very short deadtime, no convolution of the acquired signal with T_2^*, and the possibility of quantitative T_2^* and spin density mapping of fast-relaxing signals. There are, however, a number of serious difficulties encountered with SPRITE that must be overcome before the method is suitable for in vivo application and before it becomes competitive with established methods such as FLASH and projection imaging. These disadvantages include longer acquisition times, the use of many more radiofrequency pulses than required by the conventional methods, leading to possible specific absorption rate (SAR) limitations for in vivo applications. These disadvantages need to be addressed and weighed against the advantages (such as quantitative information) of SPRITE. A detailed discussion and a comparative presentation of SPRITE with the conventional methods is, however, outside the scope of this article.

Here, sodium density maps acquired using three SPRITE-based methods, i.e., Standard-SPRITE, Spiral-SPRITE, and Conical-SPRITE, have been compared in terms of the resulting qualitative and quantitative information as well as acquisition times.

2. Theory

2.1. Single point and SPRITE imaging

Single point imaging (SPI) methods have been demonstrated to be ideal for imaging systems having short relaxation times [15–18]. SPI is a pure phase encode technique, without a readout gradient, as the k-space is encoded through repetitive and brief (broadband, non-selective) RF pulses applied in the presence of phase encode gradients. Following each RF excitation, a single datum point is acquired at an encoding time, t_p. Due to the very short encoding times and the single point data acquisition, the images obtained using SPI methods are free from artefacts originating from B_0 inhomogeneity, susceptibility variations, and chemical shift [19].

The SPI method, however, suffers from long acquisition times and is also very demanding in terms of hardware due to the fast gradient switching which induces strong vibrations in the scanner. To decrease the acquisition times and to avoid the hardware limitations of these techniques, Balcom et al. [20] introduced the SPRITE method. SPRITE employs the same acquisition scheme of SPI but in conjunction with a step-wise ramped primary phase encode gradient. In this way, SPRITE greatly reduces the acquisition times, the gradient switching required and consequently allows for more rapid image acquisition without excessive gradient vibration [20]. Further, the acquisition times and gradient duty cycles induced by SPRITE have been significantly reduced by introducing alternative k-space trajectories such as in the Spiral-SPRITE and Conical-SPRITE sequences [21] which, being implementations of centrically ordered k-space sampling schemes, also increase the sensitivity. In Fig. 1 the timing diagrams of the three sequences are presented.

Unfortunately, SPRITE imaging techniques, independent of which k-space trajectory is used, are inefficient imaging techniques as just a single complex datum point is acquired after each RF excitation. For this reason, to obtain good SNR, scans have to be repeated several times with a consequent increase in acquisition time. To circumvent this problem, a solution which involves the acquisition of multiple FID data points following each RF excitation for the SNR enhancement [22] has been implemented. This possibility arises from the fact that in SPRITE sequences, after the acquisition of a single point, the acquisition system waits until the end of the current TR without any activity. Acquisition of multiple FID points is thus of particular importance where acquisition times have to be reduced to a minimum, i.e., in all in vivo applications.

2.2. Multiple FID point acquisitions

The signal associated with a single datum point acquired at an encoding time, t_p, in the presence of constant phase encode gradient, $\mathbf{G}$, is given by

$$S(\mathbf{k}) = \int\int\int \rho_{app} \sin\alpha \, e^{-\frac{t_p}{T_2^*}} e^{-i2\pi\mathbf{k}\cdot\mathbf{r}} \, d\mathbf{r}, \tag{1}$$

where

$$\mathbf{k} = \frac{1}{2\pi}\gamma\mathbf{G}t_p, \tag{2}$$

α is the flip angle, γ is the gyromagnetic ratio and ρ_{app} is the apparent nuclei density including all sampling and longitudinal magnetization relaxation effects. From Eqs. (1) and (2) it is apparent that the acquisition of multiple data FID points will have a consequence in the T_2^* weighting of the signal. The T_2^* weighting of the FID points can be used to create T_2^* mapping applications or can be minimized through the selection of short dwell times if signal averaging is required. However, since the acquisition of the multiple points takes place in the presence of active phase encoding gradients, during a complete scan an entire set of k-space data points is acquired for each value of t_p. Each of these data sets, with a k-space step size unique to

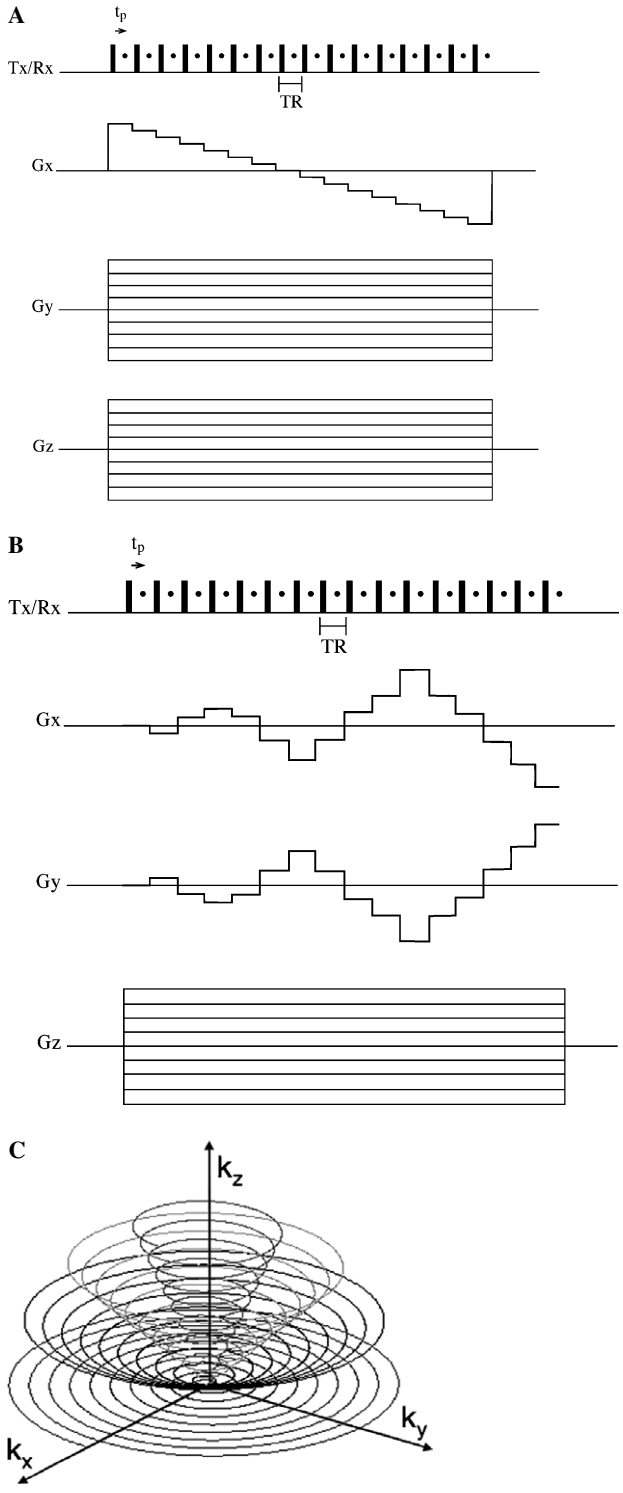

Fig. 1. (A) SPRITE imaging sequence. (B) Spiral-SPRITE pulse sequence. Each gradient step corresponds to a sample excitation using a broadband RF pulse. The gradients are sinusoidally ramped through a discrete set of gradient amplitudes for each spiral. (C) A system of four conical trajectories nested to form the top half of a sphere in k-space. Four cones are chosen for ease of illustration. In practice 39 cones were implemented for Conical-SPRITE.

each t_p, can be reconstructed into a complete image. The FOV of any one of these images is inversely proportional to the k-space step size, Δk, and thus to t_p, by

$$\mathrm{FOV} = \frac{1}{\Delta k} = \frac{2\pi}{\gamma \Delta G t_p}. \tag{3}$$

The result of a SPRITE experiment with multiple FID point acquisition is therefore a set of complete images, each weighted by the T_2^* decay and each with slightly different field-of-view. Prior to image recombination, a Chirp-z transform algorithm has been used to scale the fields of view [22].

2.3. Signal averaging of multiple FID point images

To obtain a true SNR enhancement of the images using SPRITE with the multiple FID point acquisition scheme, two conditions have to be fulfilled. The first is that the dwell time, Δt_p, must be sufficiently large to avoid noise correlation in images reconstructed from successive FID points and the second is that the extent of FOV scaling must be limited to maintain an acceptable resolution.

It has been shown before [22] that in order to accomplish the first condition the dwell time between FID points must be greater than the inverse of twice the filter width, i.e.,

$$\Delta t_p \geqslant \frac{1}{2\mathrm{FW}}. \tag{4}$$

Combining this equation with the condition for the filter width obtained by Gravina and Cory [19] the expression for the optimal dwell time for a multiple acquisition can be obtained:

$$\Delta t_p \geqslant \frac{2t_p}{n}, \tag{5}$$

where n is the of largest number of phase encode steps of the acquisition matrix. Eq. (4) can be used to determine the minimal duration of the acquisition time window, T, necessary to acquire m multiple FID points, i.e.,

$$T = \frac{2t_p}{n}(m-1). \tag{6}$$

From this relation, the maximum number of acquirable FID data points, given the dwell time and an empirical maximum allowed zooming factor, Z_{lim}, can be determined

$$m \leqslant \frac{n}{2}\left(\frac{1}{Z_{\mathrm{lim}}} - 1\right) + 1. \tag{7}$$

Since Eq. (7) gives the number of multiple points independently of the initial encoding time, a short initial encoding time can be chosen to minimize the signal loss due to the T_2^* decay. This particular feature of the multiple FID acquisition is obviously extremely powerful for imaging fast-decaying nuclei such as sodium, for example.

3. Methods

Three SPRITE sequences and their variants Standard, Spiral, and Conical, all with multiple FID point acquisitions were implemented on a Varian 4T Unity *Inova* system

(Palo Alto, CA) equipped with Siemens (Erlangen, Germany) Sonata whole-body gradients capable of a maximum gradient strength of 40 mT/m and peak slew rate of 200 mT/m/s. The RF probe was a home-built, 8-element quadrature birdcage coil of 26 cm diameter tuned for ^{23}Na. All images were acquired with NEX = 32 conventional averages using a 3D matrix size of $32 \times 32 \times 16$ k-space points and a field-of-view of $256 \times 256 \times 160$ mm corresponding to a nominal resolution of $8 \times 8 \times 10$ mm.

Identical acquisition parameters were used for every SPRITE variant. The encoding time was $t_p = 180$ μs while the repetition time was TR = 1.0 ms and the flip angle = 2°. Furthermore, in order to enhance the SNR, after each RF excitation pulse we acquired $m = 5$ multiple FID points separated by a dwell time of 12 μs in each of the 32 scans. The maximum allowed zooming factor was set to $Z_{lim} = 0.8$.

The total acquisition times varied significantly for the three SPRITE imaging sequences. The Standard-SPRITE acquisition was the longest and took 3809 s (63 min and 29 s). The Spiral- and Conical-SPRITE sequences, as expected, were significantly faster and resulted in total acquisition times of 440 and 235 s, respectively. The acquisition time reduction originates from the fact that not all the points of the k-space defined by Standard-SPRITE are acquired in the Spiral and Conical variations. For a complete discussion of acquisition time reduction and other aspects of centric SPRITE methods we refer the reader to [21].

Data averaging was performed in three consecutive steps. In the first step, the acquired scans were averaged in the normal way by summing up the scans to obtain a single, averaged dataset. In the second step, this dataset was separated into m different sub-datasets corresponding to every datum point sampled during the FID and finally, in the third step, the sub-datasets were transformed using the Chirp-z transform into images having a common FOV. At this point the images were then averaged in image space to obtain the final result.

Using the multiple FID points acquisition is equivalent to increase the number of scan averages (NEX) by a factor of m in the same acquisition time of a normal averaged scan. In the present work, for example, having acquired NEX = 32 scans and $m = 5$ multiple points we obtained an equivalent number of scans $NEX_{eq} = NEX \cdot m = 160$ scans.

All experiments were performed on an ensemble of homogeneous agarose gel phantoms with ^{23}Na concentrations ranging from a minimum of about 40 mM to a maximum of about 250 mM. The agarose concentration was also varied in order to obtain phantoms with differing relaxation characteristics. The gel phantom containers had a cylindrical shape all with the same dimensions of 60 mm in diameter and 10 mm in height.

The precise total sodium concentration of each sample was obtained by Inductively Coupled Plasma Optical Emission Spectral (ICP-OES) analysis from specimens of 100 mg. Before the analysis took place, each specimen was first mixed with 0.5 g of lithium borate and heated up to 1000 °C in 10 h and kept at this temperature for 4 h. The resulting fusion was dissolved in 50 ml HCl (3%) and then mixed with water before being fed into the plasma. In addition, all phantoms were characterized separately by bulk relaxation measurements. In particular, the slow and fast components of the sodium T_2^* decay were obtained by fitting an FID acquired after a $\pi/2$ excitation pulse with a bi-exponential model. T_1 relaxation measurements were performed by measuring the spectrum peak intensities of a typical π-τ-$\pi/2$ sequence with variable delays τ. The measured peak intensities were plotted against τ and a simple mono-exponential model was used to fit the curves (it is noted that in reality T_1 is also bi-exponential, however in this particular case we are just interested in an estimation of its average value). Table 1 shows the complete list of the phantom compositions and relaxation parameters.

Table 1
Phantom properties and relaxation times

Sample	[Na] [mM]	[Ag] [w%]	$T^*_{2\,fast}$ [ms]	$T^*_{2\,slow}$ [ms]	T_1 [ms]
1	43.5	3	2.65 ± 0.02	8.54 ± 0.02	37.2 ± 0.6
2	78.3	2	4.47 ± 0.02	9.75 ± 0.02	41.6 ± 0.4
3	113.0	1	4.3 ± 0.1	13.9 ± 0.5	48.1 ± 0.3
4	134.8	4	2.83 ± 0.02	9.32 ± 0.02	36.4 ± 0.5
5	173.9	2	3.77 ± 0.02	11.82 ± 0.03	44.2 ± 0.4
6	200.0	5	2.45 ± 0.02	9.48 ± 0.02	33.0 ± 0.2
7	234.8	3	3.61 ± 0.02	10.57 ± 0.02	38.3 ± 0.2

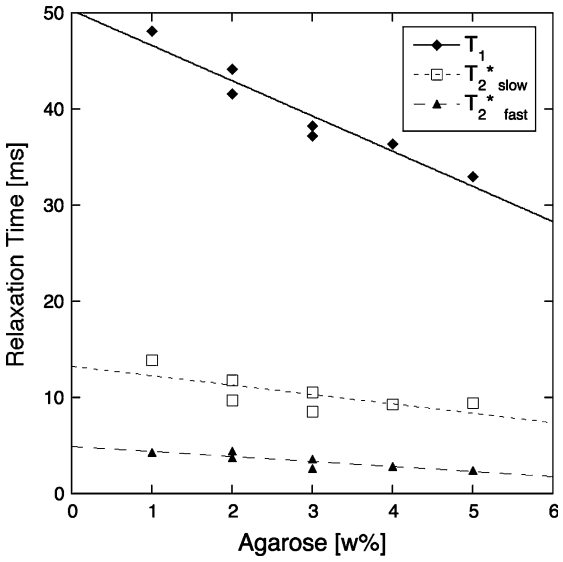

Fig. 2. Plot of the homogeneous agarose gel phantoms relaxation parameters obtained by bulk measurements. A clear linear dependence of the parameters as a function of the agarose concentration is observed.

Fig. 2 shows the plots of the measured relaxation parameter as a function of the agarose content. A clear linear dependence is observable for both T_1 and T_2^* relaxation parameters.

3.1. In vivo ^{23}Na SPRITE imaging

To demonstrate the feasibility of ^{23}Na SPRITE imaging in vivo, a Conical-SPRITE acquisition of the brain of a

healthy volunteer was carried out. The acquisition parameters were as follows: FOV = 240 × 240 × 240 mm, acquisition matrix of 32 × 32 × 32 (voxel volume of 422 mm^3), TR = 1 ms, $t_p = 0.5$ ms, $\alpha = 3°$, $Z_{lim} = 0.67$, $m = 9$ multiple points, sw = 29 kHz, NEX = 150, total acquisition time ~30 min. The average power deposition was monitored during the scan and was kept well under the regulatory limit of 8 W/kg for local RF irradiation. It is worth noting that using this multi-point acquisition, the equivalent number of scan averages, given NEX = 150 and $m = 9$, was $NEX_{eq} = NEX \cdot m = 1350$.

4. Results and discussion

Fig. 3 shows the central sections of the 3D ^{23}Na images obtained using (A) Standard-SPRITE, (B) Spiral-SPRITE, and (C) Conical-SPRITE sequences. All images were acquired using the multiple FID data sampling scheme and to the same data processing was applied to each image. In this way, the images show the differences introduced by the characteristics of the three sequences.

From these images it can be immediately seen that the image quality, as determined visually from the background noise and edge definition, increases as we move from the Standard-SPRITE technique toward the centric versions of SPRITE. The origin of this effect is due to the particular *k*-space trajectory followed during the acquisition. A more precise investigation of image quality requires the use of a ''resolution phantom'' with structures of known size in it. Measurement of such small structures, however, is difficult with sodium since the SNR is usually low.

In the Standard-SPRITE case (Fig. 3A), the *k*-space is sampled starting from one extreme and progresses line-by-line towards the opposite edge crossing the *k*-space centre once during the whole acquisition. In addition, the acquisition of the centre of *k*-space takes place in the presence of a steady-state longitudinal magnetization which determines a loss of available signal. As a result, the general SNR is low and the sample with the smallest sodium concentration (43.4 mM) is not clearly visible. Only a detailed inspection of the image reveals the presence of signal in the area occupied by this sample. However, as the inspected samples increase in sodium concentration, the signals increase proportionally demonstrating an acceptable sensitivity.

The image obtained from Spiral-SPRITE is shown in Fig. 3B. In this SPRITE variant, the 3D *k*-space is sampled through a stack of planar spirals resulting in a major reduc-

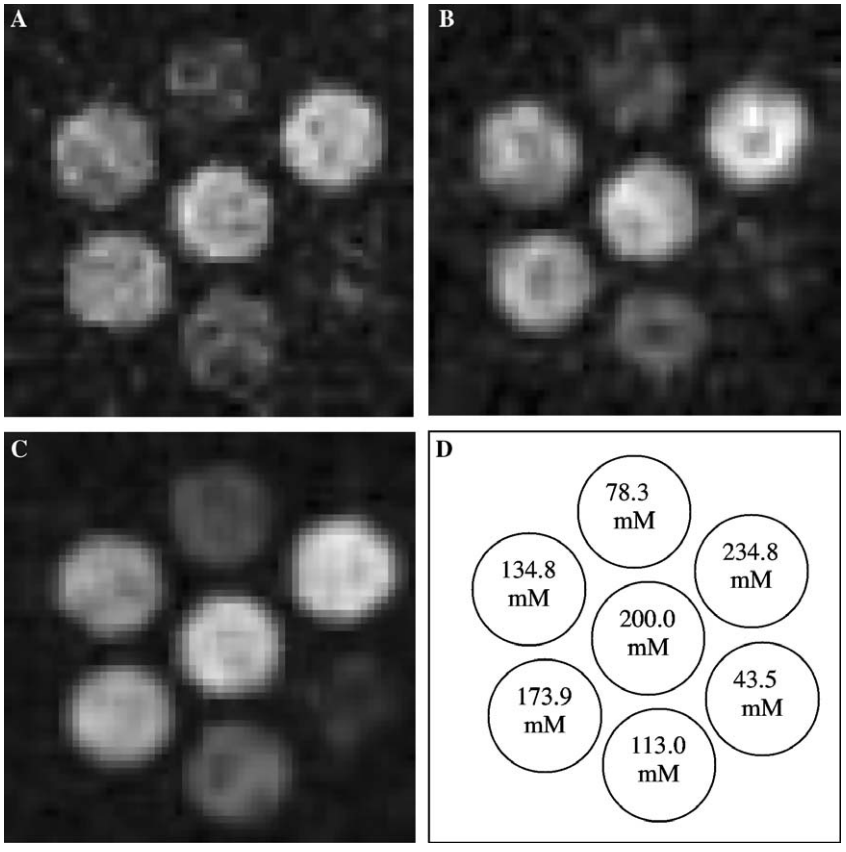

Fig. 3. Central sections of the 3D ^{23}Na images obtained using (A) Standard-SPRITE, (B) Spiral-SPRITE, and (C) Conical-SPRITE imaging sequences. (D) Schematic representation of the spatial distribution of the phantoms. All images were acquired using $t_p = 0.180$ ms, TR = 1.0 ms, and $m = 5$ multiple FID data points. The FOV was 256 × 256 × 160 and the matrix size 32 × 32 × 16. The total acquisition times were 3809 s for Standard-SPRITE, 440 s for Spiral-SPRITE and 235 s for Conical-SPRITE. The same data processing, involving rescaling with Chirp-*z* transformation, was applied to every dataset. The images show the differences resulting from acquisition with the different sequences.

tion in acquisition time (440 s) compared to the Standard-SPRITE (3809 s). The particular k-space trajectory followed by Spiral-SPRITE is not purely centric since the centre of k-space is sampled only once in combination with the central spiral of the stack. However, since the spiral trajectory always starts from the centre of a given plane, the centre of k-space is the first point sampled in the spiral trajectory and this ensures the acquisition of the whole available signal without steady-state effects due to the fast repetition of RF excitation pulses. This clearly increases the SNR considerably as can be seen by comparing the image obtained with this method and the image obtained using Standard-SPRITE. However, the signal arising from the lowest concentration sample is not yet clearly discernible, though a significant increase is observed. Finally, as for the Standard-SPRITE technique, the method shows good sensitivity allowing for a quantitative analysis of the various phantoms on the basis of their image intensity.

In Fig. 3C, the image obtained using the Conical-SPRITE technique is shown. In this case, the k-space is sampled along spiral trajectories built on the surface of cones of variable pitch angle (Fig. 1). Conical-SPRITE is the fastest sequence among the SPRITE techniques presented here and allows a time reduction of a factor of about 16 and 1.8 compared to Standard-SPRITE and Spiral-SPRITE, respectively. The acquisition time reduction in Conical-SPRITE is achieved by virtue of the fact that 16 time fewer k-space points are sampled. A detailed discussion of the reduced k-space sampling, and its consequences for the point spread function, has been presented by Halse et al. [22]. Furthermore, as this sequence acquires the centre of k-space for each and every cone as the first point and includes a delay to allow for longitudinal magnetization recovery between each cone, the SNR of the resultant images is higher than for other SPRITE sequences in a given acquisition time. In this specific case, this effect is particularly appreciable when looking at signals arising from the sample with the lowest sodium concentration which starts to be clearly visible in the image (Fig. 3C). Using Conical-SPRITE, a great sensitivity gain can be achieved. It is also noted that the level of background noise is very low. Conical-SPRITE, however, due to its particular sampling scheme introduces blurring which has been estimated from previous PSF simulations [21] to be larger than both the Standard-SPRITE and Spiral-SPRITE acquisition sequences.

From the signal equation for SPRITE sequences, Eq. (1), it can be shown that using a short TR and/or a small flip angle, ρ_{app} can be substituted by the actual sample spin density ρ [17]. In that case, using a very small encoding time, t_p, one can obtain a direct quantitative measure of the sample spin density. The choice of a very small t_p is particularly important for the quantitative characterization of sodium since it is a fast-relaxing nucleus which also shows a transverse bi-exponential decay characterized by a fast and a slow component. A short t_p will reduce losses of signal due to the fast-relaxing component of the decay.

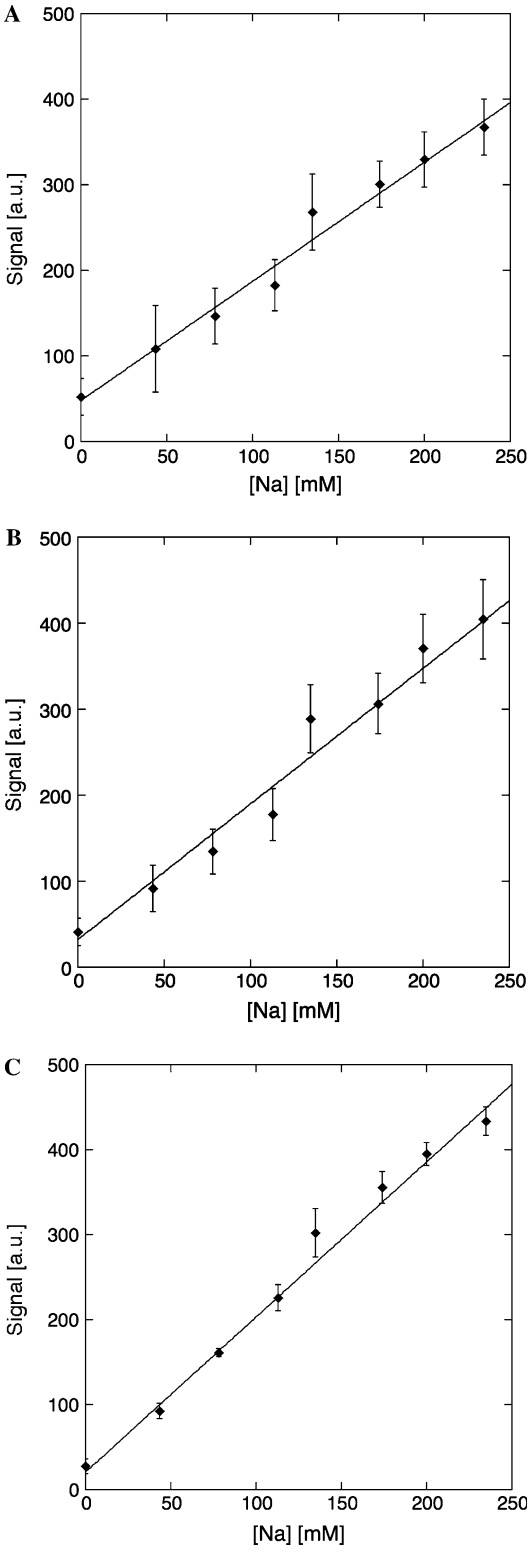

Fig. 4. Plots of the mean signal in a small region of interest as a function of the sodium concentration from (A) Standard-SPRITE, (B) Spiral-SPRITE, and (C) Conical-SPRITE images in Fig. 3. Given that the SNR is not high in those images and that the magnitude of the noise is still significant, the first datum point in each plot is the mean of the background signal. The error bars are the standard deviation of the mean intensity. A linear fit is showen for each plot. The correlation coefficients of $r = 0.99731$ for Standard-SPRITE, $r = 0.986$ for Spiral-SPRITE and $r = 0.993$ for Conical-SPRITE are indicative of a very good linear dependence.

Fig. 4 shows the plots of the signal intensity of 4×4 pixels regions-of-interest within each phantom as a function of ^{23}Na concentration. The eighth datum point in the plots is the mean intensity of the background noise in each image. From this plot, it can be observed that for all the SPRITE sequences a linear behaviour of the signal as a function of the sodium concentration has been obtained. The plots also show *quantitatively* the differences due to the three acquisition schemes. In particular, it can be seen that the signals measured in the ROIs of the images reconstructed from the Standard-SPRITE and Spiral-SPRITE acquisitions (Figs. 4A and B) have a larger variance (indicated by the error bars) compared to the Conical-SPRITE (Fig. 4C). Fig. 5 shows the plots of the SNR calculated as the ratio between the signal arising from the selected ROIs and the background noise, normalized to the concentration of the sample, the volume of the ROI and the square-root of the acquisition time. From this plot, the different sensitivity of the methods is clear and indicates that the Conical-SPRITE imaging approach is the most sensitive.

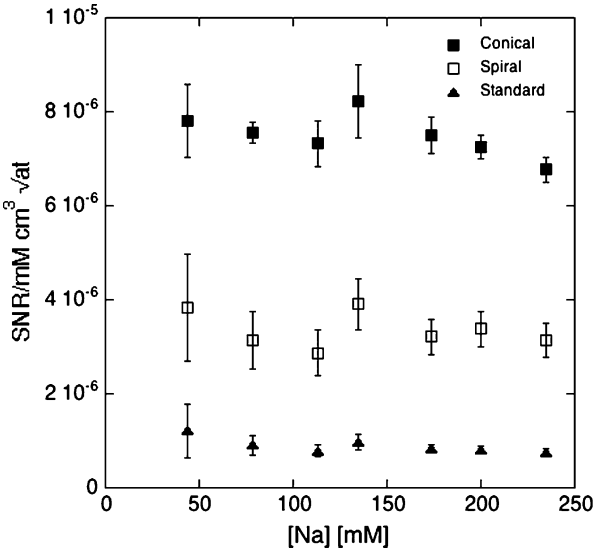

Fig. 5. Plots of the SNR calculated as the ratio between the signal arising from ROIs selected within each sample and the background noise, normalized to the concentration of the sample, the volume of the ROI and the square-root of the acquisition time. The plot shows clearly the differences in sensitivity of the methods. In particular, Conical-SPRITE shows the highest sensitivity across all the samples.

4.1. In vivo ^{23}Na images

Fig 6. shows in vivo ^{23}Na images of the brain of a healthy volunteer acquired using Conical-SPRITE. Despite the fact that the images have been acquired with a relatively low resolution ($7.5 \times 7.5 \times 7.5$ mm voxel size) and suffer from the typical blurring introduced by Conical-SPRITE, the images readily show many anatomical details such as the ventricles, filled with cerebral spinal fluid (CSF), the eyes, the cerebellum, and the central sulcus. The scalp is also recognisable in the images. The SNR calculated from a region-of-interest centred within the ventricles gave a value of 23. The SNR in the eyes was 21 and in a region of brain tissue, which included both white matter and grey matter, it was 17. The relatively low contrast-to-noise ratio (CNR) between brain tissue and CSF (CNR = 0.7), a direct consequence of the very short encoding time ($t_p = 0.5$ ms) chosen for the acquisition, should be noted. Thus, Conical-SPRITE is suitable for sodium imaging in vivo and shows very good sensitivity to the fast-relaxing component of the typical bi-exponential signal which characterises the ^{23}Na signal in restricted environments such as brain tissue.

A comparison of SPRITE imaging methods, as presented in this work, is the first step towards the application of this type of technique for the quantification of total sodium concentration (TSC) in human brain and for possibly the mapping of T_2^* in vivo. SPRITE methods offer an elegant way to acquire images of very fast-relaxing nuclei since very short encoding times are easily achievable. Furthermore, SPRITE is insensitive to many of the problems which hinder conventional sequences, such as blurring

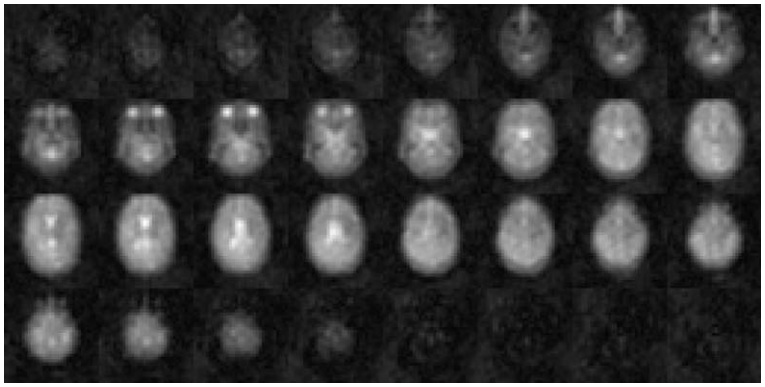

Fig. 6. In vivo Conical-SPRITE ^{23}Na imaging of a healthy volunteer brain. The acquisition parameters were as follows: FOV = $240 \times 240 \times 240$ mm, acquisition matrix of $32 \times 32 \times 32$. Voxel size $7.5 \times 7.5 \times 7.5$ mm (voxel volume of 422 mm^3), TR = 1 ms, t_p= 0.5 ms, $\alpha = 3°$, $Z_{lim} = 0.67$, $m = 9$ multiple points, sw = 29 kHz, NEX = 150, total acquisition time ~30 min. Using the multiple FID points acquisition the equivalent number of scan averages, given NEX = 150 and $m = 9$, was $NEX_{eq} = NEX \cdot m = 1350$.

due to convolution of the point spread function with the T_2^* decay during the readout time, chemical shift artefacts, or B_0 inhomogeneity. All these advantages make this method very attractive for ^{23}Na imaging. However, SPRITE imaging has several drawbacks that need to be addressed before its application in vivo will be possible. As the results of this work demonstrate, SPRITE imaging of ^{23}Na suffers from a low SNR and high noise level determined by the large spectral widths needed to acquire the signal [19]. Further, for in vivo applications in humans, the use of high flip-angle pulses will be problematic. The use of variable flip angles can help to mitigate against this [23]. For the set of experimental parameters selected for comparison of the three versions of SPRITE, the SNR for the Standard-SPRITE sequence was the lowest with values between 2 and 6 for the ^{23}Na phantoms with concentrations in the range of 43.5–235 mM. Spiral-SPRITE performed slightly better with SNR values ranging from 2.5 to 8, but in significantly shorter acquisition times. Finally, Conical-SPRITE, being a centric scan method performed better than the other SPRITE variants giving SNR values ranging from 3.5 to 16. Normalizing the SNR to the sample concentration, the square-root of the acquisition time of the three SPRITE variants, and the voxel size, it can be seen that Conical-SPRITE is the sequence with the highest sensitivity.

With an appropriate selection of SPRITE sequence, such as Conical-SPRITE, and a set of optimized parameters, such as number of multiple FID points acquired for SNR enhancement, and an appropriate number of averages, good images of ^{23}Na in vivo can be obtained in an acquisition time of approximately 30 min. This, however, is still somewhat longer than the commonly accepted limits in clinical application. However, the quantitative information content of the images could be seen as a trade-off against the lengthy acquisition time. With this longer acquisition time and through proper choice of the sequence parameters, images with a good SNR have been obtained using Conical-SPRITE. Further, with the very short encoding time used ($t_p = 0.5$ ms) a reduction of CNR between brain tissue CSF has been observed. This indicates good sensitivity of the imaging technique to the fast-relaxing component of the bi-exponential relaxation of the sodium signal.

A comparison of the SPRITE-based sequences presented here with conventional approaches for sodium imaging, such as projection reconstruction or FLASH, is difficult because of the many divergent advantages and disadvantages of the respective methods. For example, SPRITE-based methods alone are able to provide accurate and quantitative measures of the T_2^* of fast-relaxing nuclei from imaging data [15]. However, this advantage comes at the expense of higher gradient duty cycles than might be the case with conventional methods. A comparison of conventional methods with the best SPRITE-based method, Conical-SPRITE, is clearly important for future in vivo applications. This work is currently being pursued.

5. Conclusions

The suitability of the SPRITE technique for potential clinical applications, in the three different guises presented here, rests on the consideration of the quantitative information output compared with acquisition time. The Conical-SPRITE acquisition shows relatively few image artefacts and, moreover, the intensity across the homogeneous phantoms is more uniform than for the other two methods. The quantitative measure of the sodium density, as determined by the three methods, does not differ significantly; Conical-SPRITE performs slightly better. The substantial reduction in acquisition time for Conical-SPRITE compared with Standard-SPRITE is an advantage which will prove critical for clinical applications. Despite the reduced acquisition time, the quality of the fit is marginally better, and by virtue of centric scanning, the SNR is slightly improved for Conical-SPRITE. In conclusion, the overall advantages of Conical-SPRITE for potential clinical applications are: lower SAR because fewer RF pulses are needed; acquisition time reduced by a factor of ~20 over Standard-SPRITE; less sensitivity to motion artefacts and reduced demands on the gradient system.

Acknowledgments

We gratefully acknowledge support from the Deutsche Forschungsgemeinschaft (DFG: ZI 192/14-1) and the Bundesministerium für Bildung und Forschung (BMBF: 01GO0104 and 01GO0204) for support of the 4T MRI. BJB thanks the Canada Chairs Programme for a Research Chair in MRI of Materials (2002–2009). MH thanks NSERC of Canada for a post graduate scholarship, the University of New Brunswick School of Graduate Studies for a John S. Little International Study Fellowship and Forschungszentrum Jülich for a travel grant. Further, we thank Varian GmbH (Michael L. Gyngell, Uwe Köpper and Gerald Simon) for providing technical support.

References

[1] J.B. Lingrel, T. Kuntzweiler, Na^+, K^+-ATPase, J. Biol. Chem. 269 (1994) 19659–19662.
[2] P. DeWeer, in: D.W. Seldin, G. Giebisch (Eds.), The Kidney: Physiology and Pathophysiology, Raven, New York, 1985, p. 31.
[3] I.L. Cameron, N.K.R. Smith, T.B. Pool, R.L. Sparks, Intracellular concentration of sodium and other elements as related to mitogenesis and oncogenesis in vivo, Cancer Res. 40 (1980) 1493–1500.
[4] W.H. Perman, P.A. Turski, L.W. Houston, G.H. Glover, C.E. Hayes, Methodology of in vivo human sodium MR imaging at 1.5 T, Radiology 160 (1986) 811–820.
[5] F.E. Boada, J.D. Christensen, F.R. Huang-Hellinger, T.G. Reese, K.T. Thulborn, Quantitative in vivo tissue sodium concentration maps: the effects of biexponential relaxation, Magn. Res. Med. 32 (1994) 219–223.
[6] F.E. Boada, J.S. Gillen, G.X. Shen, S.Y. Chang, K.T. Thulborn, Fast Three Dimensional Sodium Imaging, Magn. Res. Med. 37 (1997) 706–715.

[7] T.B. Parrish, D.S. Fieno, S.W. Fitzgerald, R.M. Judd, Theoretical basis for sodium and potassium MRI of the human heart at 1.5 T, Magn. Res. Med. 38 (1997) 653–661.
[8] K.R. Thulborn, T.S. Gindin, D. Davis, P. Erb, Comprehensive, MR imaging protocol for stroke management: tissue sodium concentration as a measure of tissue viability in nonhuman primate studies and in clinical studies, Radiology 213 (1999) 156–166.
[9] K.R. Thulborn, D. Davis, H. Adams, T. Ginding, J. Zhou, Quantitative tissue sodium concentration mapping of the growth focal cerebral tumours with sodium magnetic resonance imaging, Magn. Res. Med. 41 (1999) 351–359.
[10] S. Koehler, C. Preibisch, M. Nittka, A. Haase, Fast three-dimensional sodium imaging of human brain, MAGMA 13 (2001) 63–69.
[11] D.B. Clayton, R.E. Lenkinski, MR imaging of sodium in the human brain with a fast three-dimensional gradient-recalled-echo sequence at 4 T, Acad. Radiol. 10 (2003) 358–365.
[12] R. Ouwerker, K.B. Bleich, J.S. Gillen, M.G. Pomper, P.A. Bottomley, Tissue sodium concentration in human brain tumours as measured with ^{23}Na MR imaging, Radiology 227 (2003) 529–537.
[13] W. Rooney, C. Springer, A comprehensive approach to the analysis and interpretation of the resonance of spins 3/2 from living systems, NMR Biomed. 4 (1991) 209–226.
[14] W. Rooney, C. Springer, The molecular environment of intracellular sodium: ^{23}Na NMR relaxation, NMR Biomed. 4 (1991) 227–245.
[15] B.J. Balcom, SPRITE imaging of short relaxation time nuclei, in: P. Blümler, B. Blümich, R. Botto, E. Fukushima (Eds.), Spatially Resolved Magnetic Resonance, Wiley-VCH, Toronto, 1998, pp. 75–86.
[16] C.B. Kennedy, B.J. Balcom, I.V. Mastikhin, Three-dimensional magnetic resonance imaging of rigid polymeric materials using single-point ramped imaging with T_1 enhancement (SPRITE), Can. J. Chem. 76 (1998) 1753–1765.
[17] S.D. Beyea, B.J. Balcom, P.J. Prado, A.R. Cross, C.B. Kennedy, R.L. Armstrong, T.W. Bremner, Relaxation time mapping of short T_2^* nuclei with single-point imaging methods, J. Magn. Reson. 135 (1998) 156–164.
[18] P.J. Prado, B.J. Balcom, I.V. Mastikhin, A.R. Cross, R.L. Armstrong, A. Logan, Magnetic resonance imaging of gases: a single-point ramped imaging with T_1 enhancement (SPRITE) study, J. Magn. Reson. 137 (1999) 324–332.
[19] S. Gravina, D.G. Cory, Sensitivity and resolution of constant-time imaging, J. Magn. Reson. Series A 104 (1994) 53–61.
[20] B.J. Balcom, R.P. MacGregor, S.D. Beyea, D.P. Green, R.L. Armstrong, T.W. Bremner, Single-point ramped imaging with T_1 enhancement (SPRITE), J. Magn. Reson. Series A 123 (1996) 131–134.
[21] M. Halse, D.J. Goodyear, B. MacMillan, P. Szomolanyi, D. Matheson, B.J. Balcom, Centric scan SPRITE magnetic resonance imaging, J. Magn. Reson. 165 (2003) 219–229.
[22] M. Halse, J. Rioux, S. Romanzetti, J. Kaffanke, B. MacMillan, I. Mastikhin, N.J. Shah, E. Aubanel, B.J. Balcom, Centric scan SPRITE magnetic resonance imaging: optimization of SNR, resolution, and relaxation time mapping, J. Magn. Reson. 169 (1) (2004) 102–117.
[23] J.B. Kaffanke, S. Romanzetti, T. Dierkes, B.J. Balcom, N.J. Shah, Turbo RF-SPRITE: methods to reduce acquisition time and SAR for in vivo applications, in: Proc. Inter. Soc. Magn. Reson. Med., Miami, FL, USA, 2005.